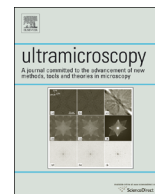




ELSEVIER

Contents lists available at ScienceDirect

Ultramicroscopy

journal homepage: www.elsevier.com/locate/ultramic

Signal-to-noise in femtosecond electron diffraction

Catherine Kealhofer^{a,b}, Stefan Lahme^{a,b}, Theresa Urban^{a,b}, Peter Baum^{a,b,*}^a Ludwig-Maximilians-Universität München, Am Coulombwall 1, 85748 Garching, Germany^b Max-Planck-Institut für Quantenoptik, Hans-Kopfermann-Str. 1, 85748 Garching, Germany

ARTICLE INFO

Article history:

Received 16 March 2015

Received in revised form

16 July 2015

Accepted 21 July 2015

Available online 22 July 2015

Keywords:

Ultrafast electron diffraction

Pump-probe techniques

4D microscopy

Femtosecond crystallography

Electron pulses

ABSTRACT

Pump-probe electron diffraction can directly record atomic-scale motion within molecules or materials. However, the available current in femtosecond experiments is limited, making it challenging to reach the sensitivity required for detecting the fastest structural dynamics, which are encoded in time-dependent diffraction intensities. Here we present a unified analysis of signal-to-noise for an ultrafast electron diffraction apparatus. We characterize the noise of realistic ultrafast electron sources and detectors, test the performance on crystalline and polycrystalline samples and discuss practical approaches for improving measurement sensitivity. The analysis is found sufficient to predict the achievable signal-to-noise ratio in pump-probe electron diffraction before actually starting an investigation.

© 2015 Elsevier B.V. All rights reserved.

1. Introduction

Ultrafast electron microscopy and diffraction [1–3] are compelling techniques for imaging atomic-scale structural dynamics with sub-angstrom and sub-picosecond resolution. The process to be investigated is initiated with an ultrafast optical pulse and subsequently probed at several delay times with an electron pulse of duration shorter than the atomic motions of interest. Repeating the experiment for different pump-probe delays provides a recording of atomic-scale dynamics in space and time.

However, space charge effects caused by Coulomb forces limit the number of electrons that can be condensed into an ultrashort pulse of a certain duration [4]. This relation is complex and constitutes one of the most essential problems in practical diffraction studies. Consequently, different regimes of ultrafast investigations have emerged. Studying irreversible processes requires few- or single-shot diffraction [5]; in this regime, microwave compression has been used to achieve 10^5 – 10^6 electrons per pulse at ~ 100 keV energy with a time resolution better than ~ 200 fs full-width at half maximum (FWHM) [6,7]. Higher energy electron sources are also promising [8–10]. Alternatively, in the few- or single-electron pulse regime [11–13], Coulomb broadening is minimized; multiple pump-probe cycles at the same time delay are integrated to measure a diffraction pattern, and higher time resolution comes at the cost of repetitive sample excitation at high repetition rate

[4,14]. Simulations predict few-femtosecond or even sub-femtosecond temporal resolution to be achievable [15,16]. The experimental feasibility of pump-probe diffraction with single-electron pulses on samples at ~ 100 kHz repetition rates has recently been demonstrated [17].

As time-resolution is pushed towards the 100 fs regime and below, practical limitations to the available average electron current occur for all of the above approaches. On one hand, Coulomb interactions create a tradeoff between pulse duration and number of electrons per pulse. On the other hand, the repetition rate at which experiments can be performed is limited fundamentally by the relaxation rate of the system under study and in practice by thermal considerations which arise from the use of thin samples. Thus the maximum repetition rate is strongly dependent on the method of excitation, thermal conduction of the sample, and quality of thermal contact to an external heat sink. This is a central problem of the technique, especially if the goal is to image the fastest atomic motions following laser excitation. The crystalline lattice spacing does not change significantly on the few-femtosecond timescale, but changes of atomic positions within the unit cell can be that fast. These are encoded in the time-dependent intensity variations of diffraction features with respect to their initial value. A careful analysis of signal-to-noise at realistic experimental conditions is therefore essential for assessing whether a certain atomic-scale dynamics will be detectable or not, given a realistic runtime of the experiment.

This paper is organized in three main parts. We first develop a simplified model for the relevant noise contributions in ultrafast imaging with typical electron sources and detectors. Second, we

* Corresponding author at: Ludwig-Maximilians-Universität München, Am Coulombwall 1, 85748 Garching, Germany.

E-mail address: peter.baum@lmu.de (P. Baum).

characterize the relevant noise parameters for the single-electron diffraction beamline of our laboratory. Third, using femtosecond electron pulses of realistic charge and repetition rate for a time-dependent study, noise is analyzed for two prototypical diffraction samples: a high quality single-crystal sample, and a weakly diffracting polycrystalline sample. We find that the measured intensity noise is described very well by the theoretical approach. In the case of a single-crystal sample, the stability of the electron source turns out to be the most decisive factor while noise contributions from the detector are negligible. This is in contrast to the case of diffraction rings, which cover a large area so that noise contributions from the detector and background become significant. In addition, we discuss some possibilities for normalizing time-dependent diffraction data with respect to the direct beam or part of the Bragg spots, which can significantly increase the signal-to-noise ratio.

2. Predicting signal-to-noise in femtosecond diffraction

Laser-induced changes of diffraction intensities can only be clearly detected if their magnitude exceeds the signal-to-noise ratio (SNR) of the experiment. In order to characterize the latter for a realistic apparatus, we consider the effects of shot noise, fluctuations of the electron source, quantum efficiency of electron detection and noise of the camera system. An uncorrelated sum of these noise contributions should provide a unified, predictive equation for the signal-to-noise ratio at realistic experimental conditions.

In a pump-probe diffraction experiment, the diffraction pattern is typically integrated for several seconds or minutes before the pump-probe delay is adjusted. To simplify the form of the equations, it is assumed that a single diffraction image is recorded for each time-step although, in practice, multiple images might be averaged. Important for the following signal-to-noise considerations is the average number $\langle N_e \rangle$ of electrons within a feature of interest in a diffraction image per delay time step. Using I_e the electron source's average current in electrons per second, T the integration time, P_{hkl} the probability for diffraction into the considered feature and η the quantum efficiency of the detector, we can estimate

$$\langle N_e \rangle \approx \eta P_{\text{hkl}} I_e T. \quad (1)$$

The average current, I_e , is the product of the average number of electrons per pulse and the repetition rate. Experimentally, $\langle N_e \rangle$ can be directly determined from a reference diffraction pattern taken with the femtosecond source. $\langle N_e \rangle$ represents the “signal” of the signal-to-noise ratio; the proportional influences of the source current, the scattering cross section and the detector efficiency are directly evident. “Noise” is defined here as the root-mean-square variation of $\langle N_e \rangle$ over an ensemble of identical measurements, i.e. for a series of diffraction patterns recorded without changing the pump-probe delay.

$$\sigma_{\text{shot}} \approx \sqrt{\langle N_e \rangle} \approx \sqrt{\eta P_{\text{hkl}} I_e T}. \quad (2)$$

Second, we allow the rate of electron emission in the femtosecond electron source to fluctuate due to instabilities. These could stem from changes in the laser parameters or changes of the photocathode's work function and morphology [18]. Typically, due to low frequency drift, the source has a noise spectrum that diverges as the frequency approaches zero. The measurement uncertainty resulting from this drift cannot be removed by averaging, but can be reduced, for example, by additional measurements of parameters correlated with the drift. This will be discussed in detail in later sections. We therefore neglect the very low frequency contributions for the time being and model the source noise as white-noise with a root-mean-square magnitude α_{source} (units of $1/\sqrt{\text{Hz}}$). As noise from different time intervals is assumed to be uncorrelated, it adds in quadrature, so that the total noise when integrating an image for a time T is

$$\sigma_{\text{source}} \approx \langle N_e \rangle \alpha_{\text{source}} / \sqrt{T} = \eta P_{\text{hkl}} I_e \alpha_{\text{source}} \sqrt{T}. \quad (3)$$

Third, the detector gain (counts-per-electron) is characterized by a mean value g and a finite rms width α_{gain} , indicating a statistical spread in the detected signal per incident electron on the detector. A finite width of the gain distribution can be a consequence of the electron multiplication processes in a phosphor or in the multiplier channels [19]. This mechanism leads to a noise of

$$\sigma_{\text{gain}} = \alpha_{\text{gain}} \sqrt{\langle N_e \rangle} / g \approx \alpha_{\text{gain}} \sqrt{\eta P_{\text{hkl}} I_e T} / g \quad (4)$$

Fourth, a diffraction feature covers a non-zero area of the detector. This can be a rather small area, as in Bragg diffraction, but it can also become very large, for example in powder diffraction or in experiments on molecules in the gas phase. Most detectors for diffraction images are pixelated devices, and the diffraction feature's intensity is here assumed to be evaluated as the sum over all digital counts in the N_{px} detector pixels defining the feature's area. For the noise of each pixel, we distinguish here two contributions. Each pixel accumulates an integration-time-dependent noise α_{int} , for example thermal noise in a charge-coupled device (CCD) or complementary metal-oxide-semiconductor (CMOS) camera, in units of (counts/s)/ $\sqrt{\text{Hz}}$. In addition, each image readout process introduces an additional noise α_{readout} that is independent of the integration time [20], for example caused by noisy readout electronics. Noise in an individual pixel is assumed to be uncorrelated with the noise of other pixels in the image. Considering the N_{px} pixels per diffraction feature, the two noise contributions are

$$\sigma_{\text{int}} \approx \alpha_{\text{int}} \sqrt{T} \sqrt{N_{\text{px}}} / g, \quad (5)$$

$$\sigma_{\text{readout}} \approx \alpha_{\text{readout}} \sqrt{N_{\text{px}}} / g. \quad (6)$$

The division by g gives these noise contributions in units of numbers of electrons, as in Eqs. (2)–(4). The total noise is obtained by assuming all five contributions to be uncorrelated, so that they add in quadrature. The signal-to-noise ratio is

$$\text{SNR} = \eta P_{\text{hkl}} I_e T / \sqrt{\sigma_{\text{shot}}(I_e, T)^2 + \sigma_{\text{gain}}(I_e, T)^2 + \sigma_{\text{source}}(I_e, T)^2 + \sigma_{\text{int}}(N_{\text{px}}, T)^2 + \sigma_{\text{readout}}(N_{\text{px}})^2}. \quad (7)$$

This noise includes fundamental and technical contributions that are modeled as follows: first, the average electron current into a diffraction feature is assumed to follow Poisson statistics. Shot noise contributes as

Some basic observations can be made from this equation. First, the integration time per image determines the relative importance of integration and readout noise. Subdividing the integration time into multiple shorter exposures does not affect the contribution of

noise terms which have a white noise spectrum (noise terms proportional to \sqrt{T}). However, this procedure increases the relative contribution of the readout noise. Different regimes appear depending on the intensity of the diffraction features. For low-intensity and/or large area diffraction features, the noise of the camera can be important. As the intensity of the diffraction feature increases, the detection noise becomes insignificant; in this regime, shot noise is dominant. Finally, because source fluctuations contribute proportional to the intensity, they overtake shot noise at large intensities. These three regimes therefore define the central points to consider in an experiment. In the following, we provide typical values for all parameters in Eq. (7) (Sections 3 and 4) and describe two experiments validating it in different diffraction regimes, crystalline (Section 5) and polycrystalline (Section 6).

3. Electron-source characterization and laser drift correction

The femtosecond electron source is driven by a Ti:sapphire long-cavity laser oscillator (Femtosource XL 500, FEMTOLASERS Produktions GmbH) delivering bandwidth-limited 60 fs pulses at 800 nm or by a Yb:YAG regenerative amplifier generating 800 fs pulses at 1030 nm [21,22]. Electron pulses are generated by two-photon photoemission from a gold photocathode using frequency-doubled optical pulses at 400 nm/515 nm wavelength. The electrons are accelerated to 30–100 keV in an electrostatic field and focused using a solenoid lens. Transmission diffraction patterns are recorded with a phosphor screen and CMOS camera (TemCam-F416, TVIPS GmbH). For structural dynamics studies, a series of diffraction images is recorded for varying time delays between an optical pump pulse and electron probe pulse.

Total measurement times can easily exceed several hours [17]; it is therefore critical to minimize long-term drifts of the experimental parameters. In particular, the average electron current must be approximately constant for the duration of the experiment. Heating the photocathode slightly using a 532 nm continuous-wave laser was found to stabilize the electron emission process from the gold film, preventing slow degradation of emittance and photoemission yield that was otherwise significant in the single-electron emission regime [17]. As the beam pointing and chirp of the laser are sensitive to changes in temperature, an additional enclosure was constructed around the laser system which damped environmental temperature fluctuations by more

than an order of magnitude. In addition, the beam pointing is actively stabilized (Aligna, TEM Messtechnik, GmbH) by using piezo-controlled mirrors to correct the beam position on a pair of quadrant detectors.

The long-term noise characteristics of the electron source were measured by removing the diffraction sample and recording 1-s images of the electron beam over a period of more than 10 h. The electron source was operated at 30 keV with an average of 1.6 electrons per pulse at a repetition rate of 2.56 MHz. The pink line in Fig. 1a shows the time-trace, and Fig. 1b depicts the resulting noise spectrum. It takes a constant value $\alpha_{\text{source}} \approx 2.6\%/\sqrt{\text{Hz}}$ above about 10^{-3} Hz and extending to the upper frequency limit of the measurement. This noise is significantly larger than the measurement noise floor or shot noise of the electron beam. On the hours-scale the current drifts are more significant and caused by changes of the laboratory environment. For example, the peak at 0.43 mHz (38 min period) corresponds to oscillations of the laboratory's air temperature by about 0.2 K rms. The source stability data is plotted in Fig. 1c in an alternate way, as relative rms fluctuations of the source vs. total measurement window. The relative rms fluctuations are evaluated for each measurement window as the standard deviation of 1-s samples of the source current, divided by the mean value of the current.

Most of the increase in noise at longer time scales is caused by drifts of the laser pulse energy, which influences the electron emission yield. In spite of the very good temperature stability of the laser enclosure, changes in laser pulse parameters can occur due to other effects, for example ageing and performance changes of the semiconductor saturable absorber mirror in the laser cavity. Recording the laser power for each diffraction image and normalizing the diffraction intensities appropriately compensates for a significant amount of drift in the photocurrent. The blue trace in Fig. 1a and b depicts the time trace and effective noise spectrum of the electron source after applying such a correction, which is in this case the square of the power in the second harmonic beam since electron emission is via a two-photon process. There is a clear improvement by up to an order-of-magnitude for measurement times longer than 10 min. Likewise, in Fig. 1c, the rms noise of the source does not diverge any more up to total experimental time windows of several hours. A more sophisticated procedure, which also compensates for drifts in the laser chirp, can also be applied [23].

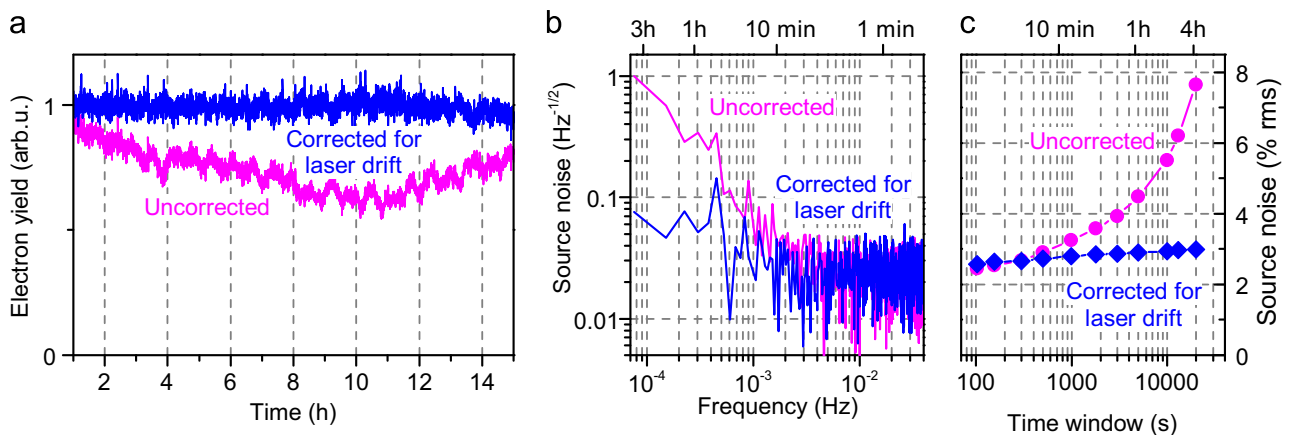


Fig. 1. Stability of a laser-driven femtosecond electron source. The pink trace is without correction, and the blue trace is with correction for changes in laser power. (a) Current vs. time. (b) Noise spectrum, i.e. relative current fluctuations per $\sqrt{\text{Hz}}$. Above about 10^{-3} Hz, the noise spectrum is flat, with a value of $2.6\%/\sqrt{\text{Hz}}$; on slower time scales, noise is much stronger. Each trace is the root-mean square average of the Fourier transforms of four time-traces of the photocurrent. (c) rms noise for different total time windows, corresponding to the source fluctuation that would be expected for different total measurement times in a diffraction experiment, with (blue diamonds) and without (pink dots) laser correction. (For interpretation of the references to color in this figure caption, the reader is referred to the web version of this paper.)

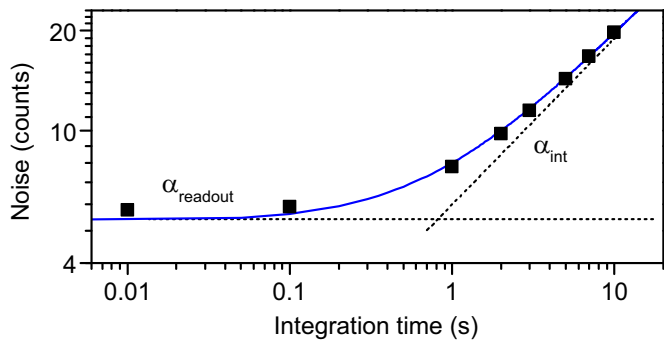


Fig. 2. Noise of a detector pixel. Black squares show the standard deviation of counts per pixel vs. the integration time; the blue line is a fit of Eqs. (5) and (6). The contributions of readout and integration noise are indicated with dotted lines. (For interpretation of the references to color in this figure caption, the reader is referred to the web version of this paper.)

4. Detector characterization

The detector in our experiment consists of a $64 \times 64 \text{ mm}^2$, $\sim 5\text{-}\mu\text{m}$ thick phosphor layer (P43) coated on a 1:1 fiber-optical bundle, which is bonded on the other side to the surface of a CMOS-based active pixel sensor chip. Additional aluminum and carbon layers prevent charging and help to reject pump light. On the chip, 4096×4096 pixels are arranged in a $15.6\text{-}\mu\text{m}$ spaced grid. The sensor can be cooled to 0°C to reduce thermal noise.

To characterize the detector's background noise, a series of images were recorded at room temperature (22.5°C) to evaluate the noise counts per pixel. Fig. 2 shows the measured standard deviation as a function of the integration time. By fitting the results using Eqs. (5) and (6), values of $\alpha_{\text{readout}} \approx 5.3 \pm 0.5$ counts/pixel and $\alpha_{\text{int}} \approx 6.0 \pm 0.1$ counts/pixel/s/ $\sqrt{\text{Hz}}$ are obtained.

At tens of keV electron energy, the electron detector is capable of single-electron detection with a quantum efficiency very close to 100% [24], i.e. the probability of not detecting an incoming electron is close to zero. Hence, the gain factor g can be determined by counting electrons. A series of 1-s images were recorded with an electron flux per pixel of less than 3×10^{-4} , so that the probability of two electrons arriving too close together to be distinguished is below 1%. The left inset of Fig. 3 shows that individual spots are clearly observable above the noise, corresponding to individual electrons hitting the phosphor. The femtosecond nature of the electron pulses makes no difference, i.e. the spots look identical to those obtained with a continuous electron beam [25]. A spot-searching algorithm based on pixels exceeding a threshold value was used to identify ~ 5000 single electron events

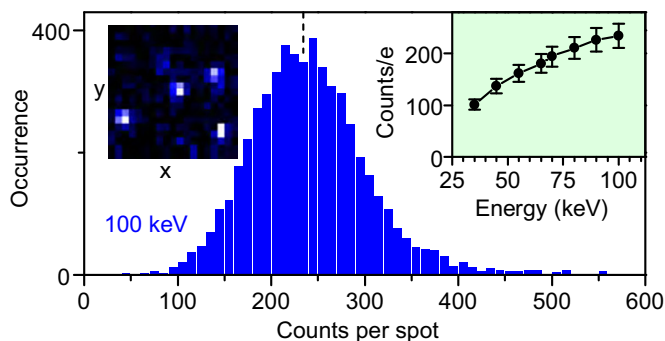


Fig. 3. Histogram of counts per electron (blue bars) based on ~ 5000 single-electron detection events. The average value (dashed line) shows the detector gain. The width of the distribution is broadened by detector noise. Left inset: an example image showing single-electron events. Right inset: gain vs. electron energy. (For interpretation of the references to color in this figure caption, the reader is referred to the web version of this paper.)

in 100 images. False positives were excluded by requiring the event to cover more than one pixel on the detector. To account for the point spread function of the detector, the number of digital counts per electron was determined by integrating a 5×5 pixel² region around the center of each identified spot. The main panel of Fig. 3 shows the resulting histogram at an electron energy of 100 keV, revealing a mean of 234 digital counts and an almost Gaussian distribution. The width of the gain distribution is significantly broadened by thermal counts from the camera due to α_{int} and α_{readout} . The data puts an upper limit of the gain width distribution of $\alpha_{\text{gain}}/g < 0.15$. The noise contribution from α_{gain} is therefore negligible in comparison to shot noise, σ_{shot} , at all conditions relevant for atomic-scale ultrafast diffraction (compare Eqs. (2) and (4)). This, however, can change for other detector schemes such a microchannel plates.

The determination of mean digital-counts per electron was repeated for electron energies down to 75 keV. For lower energies, electron counting was not reliable, and a relative calibration of integrated counts per second at constant photoemission conditions was applied. The resulting gain as a function of electron energy is shown in the right inset of Fig. 3. Towards higher energies, there is an onset of saturation, as the electrons start to penetrate the phosphor with reduced luminescence.

The spatial widths of the single-electron events also reveal the detector's spatial resolution, about 1.8 pixels or $30 \mu\text{m}$ rms. For a well-focused diffraction pattern, this high resolution facilitates determination of the spot positions; it also minimizes the number of pixels in the region of interest and hence the intensity noise.

5. Experimental noise for diffraction from a single crystal

As a first diffraction sample, we used a freestanding 40-nm film of crystalline potassium tetracyanoquinodimethane (K-TCNQ), prepared by ultramicrotomy from mm-sized single crystals obtained with a reactant diffusion technique [26]. This material system is expected to undergo an ultrafast spin-Peierls transition after laser excitation [27]. The freestanding film was mounted on a gold support mesh and its absorption spectrum and homogeneity were characterized using an optical microspectrometer [28]. The sample is large enough to comprise the collimated pulsed electron beam, which has a diameter of about $80 \mu\text{m}$.

The measurement series consists of 250 background-subtracted diffraction images measured with a 5 s integration time and an average of 10 electrons per pulse at 300 kHz repetition rate. These are feasible conditions for a pump-probe diffraction experiment with potentially few-femtosecond resolution in the few-electron regime [17], provided the excitation is reversible. In the case of an ultrafast electron diffraction experiment, the signal at a particular time delay would be taken from a *single* such diffraction image. The averaged K-TCNQ diffraction pattern is shown in Fig. 4a, revealing the layered structure of the material. The Bragg intensities cover two orders of magnitude, reflecting the complex composition of the unit cell. For signal-to-noise analysis, 28 regions of interest with a size of 25×25 pixels were defined around selected Bragg spots (see the Miller indices in Fig. 4a). In addition, to simulate Bragg spots with very low intensity, five additional regions were defined close to the central beam, where signal is dominated by inelastic scattering. The noise of each region was calculated as the standard deviation of counts over the set of 250 images.

The resulting signal-to-noise ratio (SNR) for each Bragg spot is plotted in Fig. 4b as black dots vs. the average number of electrons for each Bragg spot. The results reveal an increase of the signal-to-noise ratio with increasing Bragg spot intensity. However, there is also an evident deviation from the shot noise limit (blue dashed

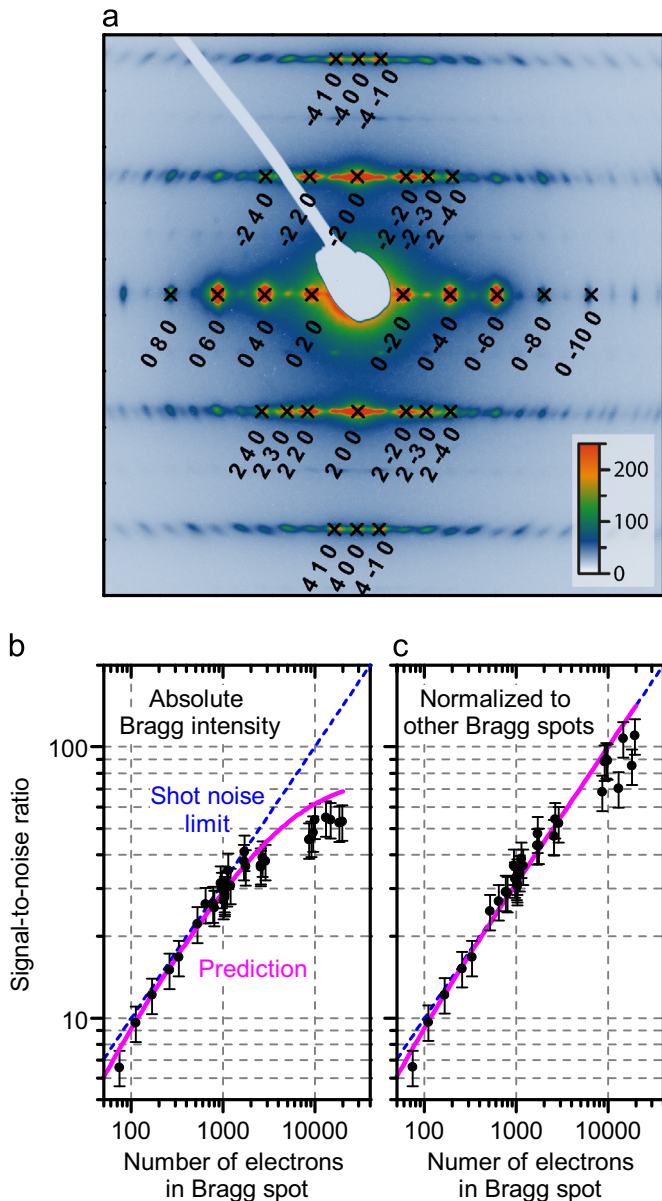


Fig. 4. Signal-to-noise analysis of a realistic pump-probe diffraction scenario with a single-crystalline sample. (a) Diffraction pattern of the organic crystal K-TCNQ recorded with ultrashort single-electron pulses. (b) Signal-to-noise ratio (black dots) for different Bragg spots in comparison to shot noise (blue dashed line) and the model prediction (pink). (c) Signal-to-noise ratio (black dots) in case of normalizing the diffraction pattern using the sum of the intensities of the remaining Bragg spots. The model prediction (pink) approaches shot noise (blue dashed line) in this case. (For interpretation of the references to color in this figure caption, the reader is referred to the web version of this paper.)

line), strongest at lowest and highest electron numbers.

The pink solid line in Fig. 4b depicts the signal-to-noise ratio predicted by Eq. (7), using the parameters obtained in the previous sections. The model quantitatively captures the experiment, including the deviations from shot noise both at low and high Bragg spot intensities. At low intensities, the thermal noise of the camera is significant. As the number of electrons increases, shot noise dominates. At even higher intensities, the signal-to-noise ratio saturates due to the electron source fluctuations. The experimental saturation occurs slightly earlier than predicted by the model. This is because the model only uses the white noise contribution to source fluctuations, neglecting low-frequency drift. Nevertheless, the agreement with the model is good.

The results of Fig. 4b have clearly identified the stability of the electron source as the main limitation for improving signal-to-noise in ultrafast electron diffraction from single-crystal samples. As long as the major component of the source fluctuations is proportional to the intensity, increasing electron current at a constant overall data-acquisition time will not push the overall noise below that of the electron source. Stabilizing the electron source is therefore a key prerequisite to a femtosecond diffraction study. The reported improvements, namely cathode heating and correction for the correlation between laser drifts and electron emission, were crucial to enabling ultrafast electron diffraction with sensitivity to few-percent intensity changes [17].

Still, there is desire for further improvement. To obtain the most information, one would like to independently measure the number of electrons in each pulse. This is impractical at high repetition rates. The next best solution would be to measure the number of incident electrons for each image. In practice, most of the current is in the direct beam, which could be used to normalize the diffraction pattern. This would capture all drifts of the electron source, including intrinsic changes and not only those correlated to the laser parameters. Measuring the direct electron beam simultaneously with the diffraction pattern is challenging because of the several orders-of-magnitude difference in current and limited dynamic range of available detectors. This problem could be addressed, however, by using a secondary detector such as a single photodiode or phosphor with attenuation in place of the beam block.

Here, as a proof of principle, we consider improving signal-to-noise by averaging the total intensity of the diffraction pattern itself to normalize for photocurrent fluctuations. This can only work if the whole pattern's added noise is significantly lower than that of each Bragg spot. The effective information in pump-probe diffraction is somewhat reduced by such a normalization procedure, but depending on the ultrafast physics to be investigated, this might well be offset by reduction of noise in the remaining observables.

Fig. 4c shows the result for the case of single-crystal diffraction from K-TCNQ. Each Bragg spot intensity has been corrected using the average over the remaining Bragg spots in the pattern. There is a clear improvement with respect to the result of Fig. 4b with only the laser-drift correction. Especially at higher Bragg intensities, the achieved signal-to-noise ratio is almost indistinguishable from shot noise (blue dashed line).

6. Experimental noise for a polycrystalline sample

As a second example of noise in diffraction, we consider a polycrystalline sample. In this case, the noise analysis is qualitatively different, because the diffraction consists of rings that cover a much larger area of the detector. In addition, the total cross section for diffraction is reduced, because only a fraction of grains within the sample volume is oriented correctly. The background from inelastic and elastic scattering becomes important for signal-to-noise.

The sample investigated is few-layer graphene (Ted Pella, Inc.) mounted on a 2000 mesh TEM grid. Thirty diffraction patterns were recorded using an electron energy of 90 keV and an exposure time of 15 s. The incident electron flux on the sample was 3 electrons per pulse at 50 kHz repetition rate. This lower repetition rate was chosen to simulate pump-probe conditions for samples with higher required pump pulse energy or lower thermal conductivity than graphite [17].

The average of the diffraction images is shown in Fig. 5a. In Fig. 5b, the distribution of scattering angles (i.e. the diffraction intensity per pixel vs. radius) is shown. The contribution from the

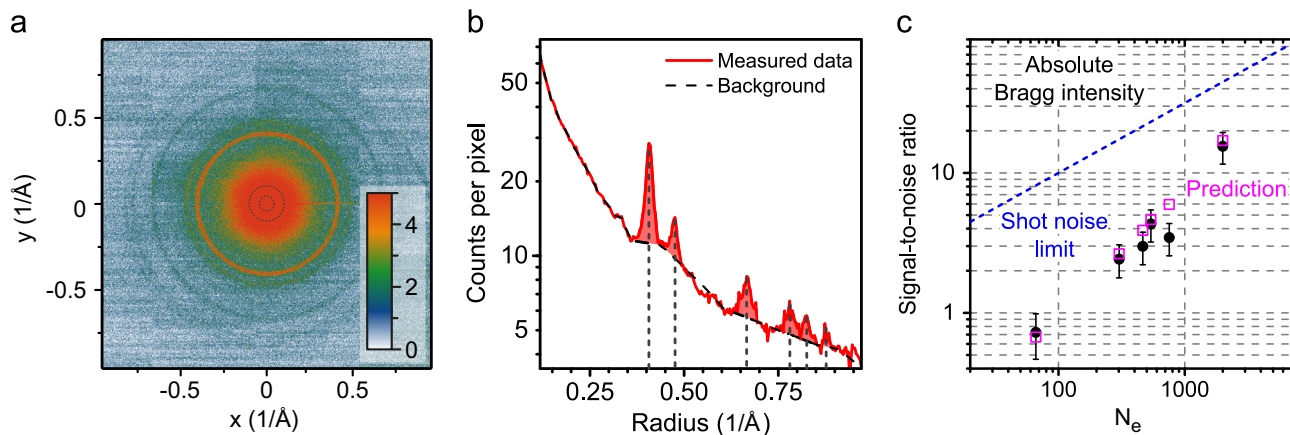


Fig. 5. Signal-to-noise analysis of a realistic pump-probe diffraction scenario with a polycrystalline few-layer graphene sample. (a) Average diffraction pattern from, with color scale indicating counts per pixel. The region used for normalizing the images is shown with a dotted line. (b) Counts per pixel vs. radius. The interpolation used for background subtraction is shown as a dashed line. The elastic diffraction signal is the area between the measurement and the background interpolation, within regions of interest defined as ± 59 pixels for the three innermost rings and ± 47 , ± 41 , ± 29 pixels for the subsequent rings of increasing radius. (c) Signal-to-noise ratio (black dots) for the six diffraction rings in comparison to shot noise (blue dashed line) and the model predictions (pink). The signal-to-noise ratio depends on both N_e and the size of the region of interest. (For interpretation of the references to color in this figure caption, the reader is referred to the web version of this paper.)

background is estimated by piecewise linear interpolation of the diffraction intensity between points selected away from the peaks. The “signal” for signal-to-noise analysis is determined as the integral of the counts above the fitted background within regions of varying ring width, indicated in Fig. 5b. In total, roughly 0.2% of the incoming electrons are elastically scattered into the diffraction rings.

Images were recorded without a beam block to allow direct measurement of the electron beam intensity. For normalization to the fluctuating electron current, the intensity detected in a donut-shaped part of the beam is used in order to exclude possible saturation in the center of the images, as shown in Fig. 5a. The signal-to-noise ratio is determined as before by considering the root-mean-square fluctuations of the number of counts in the six most intense rings in the image. The prediction from Eq. (7), based on the number of pixels in each ring-shaped region of interest, is depicted in Fig. 5c as the pink squares. The fair agreement demonstrates again the value of the framework developed here for noise analysis.

The two most dominant effects to noise in the case of polycrystalline samples are thermal detector noise and increased shot noise due to inelastically scattered electrons. These two effects, together with the typically strongly reduced diffraction efficiency, make the polycrystalline regime of time-resolved diffraction significantly more difficult than the single-crystal regime. If studying diffraction rings really cannot be avoided, it is crucial to use a detector with high gain and low thermal noise. Rings should be made as sharp as possible in order to avoid excessive area of integration. Ideally, inelastic scattering background is filtered out by energy selection [29] or single-electron events are counted individually [25].

7. Discussion

From these results we can derive a few points worth mentioning. For a single-crystal sample, the noise of the electron source is typically the most significant contribution; this noise source is instrumental and not fundamental, and indicates that better performance can be achieved. A highly stable current of femtosecond electron pulses is therefore key to advancing ultrafast electron imaging to novel sensitivity regimes. Averaging multiple frames (at each time-delay) that have been measured at different

times in the experimental sequence can help to mitigate the effect of slow drifts. However, assuming a fixed total measurement time, this procedure can only be applied to a certain extent because the required readout time per image decreases the duty ratio for data acquisition. Post-correction using measured laser parameters or, better, an independent measure of the photocathode current can further improve the sensitivity of the experiment to small changes in diffraction intensities. For polycrystalline samples with low input electron flux, cooled detectors or single-electron counting devices are required. The gain (counts-per-electron) should be set as high as permissible by the dynamic-range of the diffraction pattern. It is helpful to produce the sharpest possible diffraction rings in order to reduce the number of pixels involved in data evaluation.

In choosing the sample thickness for ultrafast electron diffraction, one must take into consideration the optical depth for the pump beam to ensure uniform pumping. There is an optimum electron energy depending on sample thickness and morphology. The lower the energy the higher the scattering cross section, but the larger the energy the lower the detector noise in comparison to shot noise.

Either phosphor screens or microchannel plates are typically applied in ultrafast electron diffraction. In terms of signal-to-noise in femtosecond diffraction, an advantage of the phosphor screen is the higher quantum efficiency, here 100% as compared to 50–80% in typical microchannel plates. This makes these detectors an effective approach for crystalline diffraction samples. On the other hand, microchannel plates can provide higher gain, and the gain can also be adjusted, providing advantages for diffuse diffraction patterns. If the microchannel plate is not operated in the space-charge saturated regime, its gain distribution is usually broader than a simple phosphor [30,31], leading to additional detection noise. In both cases, the framework outlined here allows a serious comparison of detector concepts for different applications in ultrafast diffraction.

The applicability of femtosecond electron diffraction continues to grow with the development of high coherence femtosecond sources such as laser-triggered emission from nanoscale photocathodes [32,33] or cold gases [34,35]. Such sources have already been used for ultrafast low-energy electron diffraction and selected-area diffraction [36,37], and tip sources are expected to deliver shorter electron pulses without compression [38,12]. At the same time, single-electron pulse-compression has been proposed

to reach few-femtosecond and even sub-femtosecond time resolution [15,16]. In all these emerging regimes, electrons will be scarce and consideration of signal-to-noise therefore essential. The analysis shown here can predict the achievable signal-to-noise ratio in a time-resolved diffraction study before actually beginning an experiment. This will help to spread the technique and guide the development of novel electron sources and detectors optimized for ultrafast pump-probe resolution of primary reaction dynamics.

Acknowledgements

This work was supported by the European Research Council, the Rudolf-Kaiser-Foundation and the Munich-Centre of Advanced Photonics. We thank Ferenc Krausz for support and helpful discussions and Alexander André for help with the samples.

References

- [1] D.J. Flannigan, A.H. Zewail, 4D electron microscopy: principles and applications, *Acc. Chem. Res.* 45 (10) (2012) 1828–1839, <http://dx.doi.org/10.1021/ar3001684>.
- [2] D. Shorokhov, A.H. Zewail, 4D electron imaging: principles and perspectives, *Phys. Chem. Chem. Phys.* 10 (20) (2008) 2879–2893, <http://dx.doi.org/10.1039/b801626g>.
- [3] G. Sciaini, R.J.D. Miller, Femtosecond electron diffraction: heralding the era of atomically resolved dynamics, *Rep. Prog. Phys.* 74 (9) (2011) 096101, <http://dx.doi.org/10.1088/0034-4885/74/9/096101>.
- [4] B.J. Siwick, J.R. Dwyer, R.E. Jordan, R.J.D. Miller, Ultrafast electron optics: propagation dynamics of femtosecond electron packets, *J. Appl. Phys.* 92 (3) (2002) 1643–1648, <http://dx.doi.org/10.1063/1.1487437>.
- [5] R.J.D. Miller, Femtosecond crystallography with ultrabright electrons and x-rays: capturing chemistry in action, *Science* 343 (6175) (2014) 1108–1116, <http://dx.doi.org/10.1126/science.1248488>.
- [6] T. van Oudheusden, P.L.E.M. Pasmans, S.B. van der Geer, M.J. de Loos, M.J. van der Wiel, O.J. Luiten, Compression of subrelativistic space-charge-dominated electron bunches for single-shot femtosecond electron diffraction, *Phys. Rev. Lett.* 105 (2010) 264801, <http://dx.doi.org/10.1103/PhysRevLett.105.264801>.
- [7] M. Gao, Y. Jiang, G.H. Kassier, R.J.D. Miller, Single shot time stamping of ultrabright radio frequency compressed electron pulses, *Appl. Phys. Lett.* 103 (3) (2013) 033503, <http://dx.doi.org/10.1063/1.4813313>.
- [8] S. Tokita, S. Inoue, S. Masuno, M. Hashida, S. Sakabe, Single-shot ultrafast electron diffraction with a laser-accelerated sub-MeV electron pulse, *Appl. Phys. Lett.* 95 (11) (2009) 111911, <http://dx.doi.org/10.1063/1.3226674>.
- [9] Y. Murooka, N. Naruse, S. Sakakihara, M. Ishimaru, J. Yang, K. Tanimura, Transmission-electron diffraction by MeV electron pulses, *Appl. Phys. Lett.* 98 (25) (2011) 251903, <http://dx.doi.org/10.1063/1.3602314>.
- [10] R.K. Li, P. Musumeci, Single-shot MeV transmission electron microscopy with picosecond temporal resolution, *Phys. Rev. Appl.* 2 (2) (2014) 024003, <http://dx.doi.org/10.1103/PhysRevApplied.2.024003>.
- [11] V.A. Lobastov, R. Srinivasan, A.H. Zewail, Four-dimensional ultrafast electron microscopy, *Proc. Natl. Acad. Sci. U.S.A.* 102 (20) (2005) 7069–7073, <http://dx.doi.org/10.1073/pnas.0502607102>.
- [12] M. Aidelsburger, F.O. Kirchner, F. Krausz, P. Baum, Single-electron pulses for ultrafast diffraction, *Proc. Natl. Acad. Sci. U.S.A.* 107 (46) (2010) 19714–19719, <http://dx.doi.org/10.1073/pnas.1010165107>.
- [13] A.H. Zewail, Four-dimensional electron microscopy, *Science* 328 (2010) 187–193, <http://dx.doi.org/10.1126/science.1166135>.
- [14] P. Baum, On the physics of ultrashort single-electron pulses for time-resolved microscopy and diffraction, *Chem. Phys.* 423 (0) (2013) 55–61, <http://dx.doi.org/10.1016/j.chemphys.2013.06.012>.
- [15] E. Fill, L. Veisz, A. Apolonski, F. Krausz, Sub-fs electron pulses for ultrafast electron diffraction, *New J. Phys.* 8 (11) (2006) 272, <http://dx.doi.org/10.1088/1367-2630/8/11/272>.
- [16] P. Baum, A.H. Zewail, Breaking resolution limits in ultrafast electron diffraction and microscopy, *Proc. Natl. Acad. Sci. U.S.A.* 103 (44) (2006) 16105–16110, <http://dx.doi.org/10.1073/pnas.0607451103>.
- [17] S. Lahme, C. Kealhofer, F. Krausz, P. Baum, Femtosecond single-electron diffraction, *Struct. Dyn.* 1 (3) (2014) 034303, <http://dx.doi.org/10.1063/1.4884937>.
- [18] K.L. Jensen, P.G. O'Shea, D.W. Feldman, Generalized electron emission model for field, thermal, and photoemission, *Appl. Phys. Lett.* 81 (20) (2002) 3867–3869, <http://dx.doi.org/10.1063/1.1521491>.
- [19] F.J. Lombard, F. Martin, Statistics of electron multiplication, *Rev. Sci. Instrum.* 32 (2) (1961) 200–201, <http://dx.doi.org/10.1063/1.1717310>.
- [20] H. Tian, B. Fowler, A. El Gamal, Analysis of temporal noise in CMOS photodiode active pixel sensor, *IEEE J. Solid-State Circuits* 36 (1) (2001) 92–101, <http://dx.doi.org/10.1109/4.896233>.
- [21] W. Schneider, A. Ryabov, C. Lombosi, T. Metzger, Z. Major, J.A. Fülöp, P. Baum, 800-fs, 330- μ J pulses from a 100-W regenerative Yb: YAG thin-disk amplifier at 300 kHz, and THz generation in LiNbO₃ and THz generation in LiNbO₃, *Opt. Lett.* 39 (23) (2014) 6604–6607, <http://dx.doi.org/10.1364/OL.39.006604>.
- [22] L. Kasmi, D. Kreier, M. Bradler, E. Riedle, P. Baum, Femtosecond single-electron pulses generated by two-photon photoemission close to the work function, *New J. Phys.* 17 (3) (2015) 033008, <http://dx.doi.org/10.1088/1367-2630/17/3/033008>.
- [23] S. Lahme, Femtosecond single-electron diffraction, Ph.D. thesis, Ludwig-Maximilians-Universität München, 2014, (<http://edoc.ub.uni-muenchen.de/17834/>).
- [24] M. Stumpf, K. Bobolas, I. Daberkow, U. Fanderl, T. Heike, T. Huber, C. Kofler, Y. Maniette, H.R. Tietz, Design and characterization of 16 megapixel fiber optically coupled CMOS detector for transmission electron microscopy, *Microsc. Microanal.* 16 (2010) 856–857, <http://dx.doi.org/10.1017/S1431927610054516>.
- [25] G. McMullan, A.T. Clark, R. Turchetta, A.R. Faruqi, Enhanced imaging in low dose electron microscopy using electron counting, *Ultramicroscopy* 109 (2009) 1411–1416, <http://dx.doi.org/10.1016/j.ultramic.2009.07.004>.
- [26] D.S. Acker, R.J. Harder, W.R. Hertler, W. Mahler, L.R. Melby, R.E. Benson, W. E. Mochele, 7,7,8,8-tetracyanoquinodimethane and its electrically conducting anion-radical derivatives, *J. Am. Chem. Soc.* 82 (24) (1960) 6408–6409, <http://dx.doi.org/10.1021/ja01509a052>.
- [27] H. Okamoto, K. Ikegami, T. Wakabayashi, Y. Ishige, J. Togo, H. Kishida, H. Matsuzaki, Ultrafast photoinduced melting of a spin-peierls phase in an organic charge-transfer compound, K-tetracyanoquinodimethane, *Phys. Rev. Lett.* 96 (3) (2006) 037405, <http://dx.doi.org/10.1103/PhysRevLett.96.037405>.
- [28] F.O. Kirchner, S. Lahme, E. Riedle, P. Baum, All-reflective UV-VIS-NIR transmission and fluorescence spectrometer for μ m – sized samples, *AIP Adv.* 4 (7) (2014) 077134, <http://dx.doi.org/10.1063/1.4891863>.
- [29] P. Midgley, M. Saunders, R. Vincent, J. Steeds, Energy-filtered convergent-beam diffraction: examples and future prospects, *Ultramicroscopy* 59 (1–4) (1995) 1–13, [http://dx.doi.org/10.1016/0304-3991\(95\)00014-R](http://dx.doi.org/10.1016/0304-3991(95)00014-R) Proceedings of the 2nd international workshop on Electron Energy Loss Spectroscopy and Imaging.
- [30] J.L. Wiza, Microchannel plate detectors, *Nucl. Instrum. Methods* 162 (1979) 587–601, [http://dx.doi.org/10.1016/0029-554X\(79\)90734-1](http://dx.doi.org/10.1016/0029-554X(79)90734-1).
- [31] B.R. Sandel, A.L. Broadfoot, Statistical performance of the intensified charged coupled device, *Appl. Opt.* 25 (22) (1986) 4135–4140, <http://dx.doi.org/10.1364/AO.25.004135>.
- [32] P. Hommelhoff, C. Kealhofer, A. Aghajani-Talesh, Y.R. Sortais, S.M. Foreman, M. A. Kasevich, Extreme localization of electrons in space and time, *Ultramicroscopy* 109 (5) (2009) 423–429, <http://dx.doi.org/10.1016/j.ultramic.2008.10.021>, IFES 2008 Proceedings of the 51th International Field Emission Symposium.
- [33] P. Vasa, C. Ropers, R. Pomraenke, C. Lienau, Ultra-fast nano-optics, *Laser Photon. Rev.* 3 (2009) 483–507, <http://dx.doi.org/10.1002/lpor.200810064>.
- [34] W.J. Engelen, M.A. van der Heijden, D.J. Bakker, E.J.D. Vredendregt, O.J. Luiten, High-coherence electron bunches produced by femtosecond photoionization, *Nat. Commun.* 4 (2013) 1693, <http://dx.doi.org/10.1038/ncomms2700>.
- [35] A.J. McCulloch, D.V. Sheludko, M. Junker, R.E. Scholten, High-coherence picosecond electron bunches from cold atoms, *Nat. Commun.* 4 (2013) 1692, <http://dx.doi.org/10.1038/ncomms2699>.
- [36] M. Gulde, S. Schweda, G. Storeck, M. Maiti, H.K. Yu, A.M. Wodtke, S. Schäfer, C. Ropers, Ultrafast low-energy electron diffraction in transmission resolves polymer/graphene superstructure dynamics, *Science* 345 (6193) (2014) 200–204, <http://dx.doi.org/10.1126/science.1250658>.
- [37] M.W. van Mourik, W.J. Engelen, E.J.D. Vredendregt, O.J. Luiten, Ultrafast electron diffraction using an ultracold source, *Struct. Dyn.* 1 (3) (2014) 034302, <http://dx.doi.org/10.1063/1.4882074>.
- [38] J. Hoffrogge, J.P. Stein, M. Krüger, M. Förster, J. Hammer, D. Ehberger, P. Baum, P. Hommelhoff, Tip-based source of femtosecond electron pulses at 30 keV, *J. Appl. Phys.* 115 (2014) 094506, <http://dx.doi.org/10.1063/1.4867185>.